Research paper

Highly surface electron-deficient Co_9S_8 nanoarrays for enhanced oxygen evolution

Haoxuan Zhang [a,b], Jingyu Wang [a,b], Qilin Cheng [a,b,*], Petr Saha [a,b], Hao Jiang [a,b,*]

[a] *Key Laboratory for Ultrafine Materials of Ministry of Education, Shanghai Engineering Research Center of Hierarchical Nanomaterials, School of Materials Science and Engineering, East China University of Science and Technology, Shanghai, 200237, China*
[b] *Centre of Polymer Systems, University Institute, Tomas Bata University in Zlin, Trida T. Bati 5678, Zlin, 760 01, Czech Republic*

Abstract

Tailoring valence electron delocalization of transition metal center is of importance to achieve highly-active electrocatalysts for oxygen evolution reaction (OER). Herein, we demonstrate a "poor sulfur" route to synthesize surface electron-deficient Co_9S_8 nanoarrays, where the binding energy (BE) of Co metal center is considerably higher than all reported Co_9S_8-based electrocatalysts. The resulting Co_9S_8 electrocatalysts only require the overpotentials (η) of 265 and 326 mV at 10 and 100 mA cm^{-2} with a low Tafel slope of 56 mV dec^{-1} and a 60 h-lasting stability in alkaline media. The OER kinetics are greatly expedited with a low reaction activation energy of 27.9 kJ mol^{-1} as well as abundant OOH* key intermediates (24%), thus exhibiting excellent catalytic performances. The surface electron-deficient engineering gives an available strategy to improve the catalytic activity of other advanced non-noble electrocatalysts.
© 2020, Institute of Process Engineering, Chinese Academy of Sciences. Publishing services by Elsevier B.V. on behalf of KeAi Communications Co., Ltd. This is an open access article under the CC BY-NC-ND license (http://creativecommons.org/licenses/by-nc-nd/4.0/).

Keywords: Electron deficiency; Co_9S_8; Nanoarray; Electrocatalyst; Oxygen evolution reaction

1. Introduction

Oxygen evolution reaction (OER) has been acknowledged as the core reaction of water splitting, fuel cell, CO_2 reduction, and other electrochemical processes contributed to renewable energy conversion [1–3]. The confronted OER bottleneck is sluggish kinetics with conspicuous overpotentials (η) caused by excessive adsorption strength of multiple catalytic intermediates [4,5]. It is well-reported that ruthenium (Ru)- and iridium (Ir)-based noble metal materials are highly active as OER electrocatalysts in terms of the affable adsorption towards oxygenated intermediates, yet, their scarcity and unpractical cost largely restrict the scaled-up application [6,7]. Therefore, developing high-performance

and cost-effective non-noble electrocatalysts is particularly vital to augment energy conversion efficiency in OER [8,9]. It has been well-documented that two general factors can directly determine the catalytic performances: one is the adsorption ability of metal center towards key intermediates (OOH*), and another is the charge transportation ability between the interface and bulk [10–12]. Unfortunately, it still remains a strong challenge to level both of them at the same time, thus causing inferior performances compared with noble-based electrocatalysts.

Co_9S_8 materials have been considered as an appealing and promising replacement for OER electrocatalysts, because the existence of unsaturated Co–S and metallic Co–Co can synchronously enhance OOH* intermediate adsorption on Co center at the electrochemical interface and fasten electron transportation from the surface to bulk [13–16]. In the previous literature, the synthesis of $Fe_3O_4@Co_9S_8$/rGO nanohybrid is realized by a simple solvothermal method, in which Fe

* Corresponding authors.
E-mail addresses: chengql@ecust.edu.cn (Q. Cheng), jianghao@ecust.edu.cn (H. Jiang).

introduction can facilitate Co−S break in Co−S−Co cluster to regulate the valence electron of Co center, showing a reduced overpotential of 340 mV at 10 mA cm^{-2} [17]. Besides, an N-, O-, and S-tridoped Co$_9$S$_8$ nanostructure is also reported through a pyrolysis strategy, where Co center adsorption is deeply reinforced to achieve an overpotential of 340 mV at 10 mA cm^{-2} as well [18]. Nonetheless, the presented researches aimed at activating valence electron of Co center are still limited, leading to insufficient improvement of OER performances in alkaline media.

Herein, the synthesis of highly surface electron-deficient Co$_9$S$_8$ nanoarrays is realized through a "poor sulfur" hydrothermal method, in which Co BE of the Co$_9$S$_8$ nanoarrays is significantly higher than the reported Co$_9$S$_8$ materials. When evaluated as OER electrocatalysts, the resulting Co$_9$S$_8$ can deliver current densities of 10 and 100 mA cm^{-2} at ultralow overpotentials of 265 and 326 mV, respectively, with a relatively low Tafel slope of 56 mV dec^{-1} as well as remarkable long-term stability, outperforming commercial benchmark catalysts and most of the reported Co$_9$S$_8$ materials at present. Moreover, the ECSA- and mass-normalized activities of Co$_9$S$_8$ are 0.17 mA cm^{-2} and 6.76 A g^{-1} at the overpotential of 310 mV, respectively, much higher than those of CoS (2.75 A g^{-1}; 0.10 mA cm^{-2}), also indicating superior intrinsic OER activities. Such fascinating performances are the efforts caused by high electron deficiency of the Co center in the resulting sample, which not only lowers reaction activated energy (27.9 kJ mol^{-1}), but also promotes key intermediate OOH* adsorption (24%).

2. Experimental

2.1. Synthesis of the Co$_9$S$_8$ nanoarrays

Before use, a piece of Co foam (0.6 cm × 0.5 cm × 3.0 mm) was immersed into 3 M HCl for 20 min to remove the impurities. The Co$_9$S$_8$ nanoarrays were simply prepared by a hydrothermal method. Typically, 45 mg of Co(NO$_3$)$_2$ and 10 mg of CH$_4$N$_2$S were put into 20 mL of deionized water, and the mixture was strongly stirred for 15 min to form a homogenous solution. The as-obtained solution was then transferred to a 25 mL Teflon-lined autoclave containing the clean Co foam. Subsequently, the autoclave was sealed and heated at 180 °C for 2 h. After cooled down to room temperature, the resulting sample was washed with deionized water and absolute ethanol several times. The Co$_9$S$_8$ nanoarrays were obtained after dried at 60 °C overnight in a vacuum oven. For comparison, the CoS nanoarrays were prepared with a similar procedure except that the 10 mg of CH$_4$N$_2$S was altered by 20 mg of sulfur powders.

2.2. Synthesis of the RuO$_2$ and IrO$_2$ electrocatalyst

The RuO$_2$ and IrO$_2$ powders were purchased from Adamas Reagent Co., Ltd. and Alfa Aesar with purities of 99.95% and 99.99%, respectively. In a typical synthesis, 5 mg of catalyst powder, 950 mL of isopropanol and 50 mL of 5 wt% Nafion solution were mixed by 30 min sonication to obtain well-dispersed ink. Following that, the resulting ink was dropped onto Co foam as a working elelctrode for electrochemical measurement.

2.3. Characterization

The morphology of the samples was characterized by the scanning electron microscope (SEM, Hitachi, S-4800, 15.0 kV) and transmission electron microscope (TEM, Tecnai, G2F30 S-Twin, 200.0 kV) with an energy-dispersive X-ray spectrometer (EDX), respectively. The structure of the samples was characterized by the X-ray powder diffractometer (XRD, Rigaku D/Max 2550, Cu Kα radiation, 1° min^{-1}) and X-ray photoelectron spectrometer (XPS, ESCALAB 250Xi, 40 eV, Al Kα). The contents of Co and S were measured by Inductively coupled plasma mass spectrometry (ICP-MS, Agilent 7700 spectrometer). The hydrophilic−hydrophobic properties were tested by Harke, SPCA-X-3 meter.

2.4. Electrochemical measurements

A CHI660E electrochemical workstation (CH Instruments Ins., Shanghai, China) was applied to perform all the electrochemical measurements with a standard three-electrode system containing a graphite counter electrode, a saturated Ag/AgCl reference electrode, and a 30 mL 1.0 M KOH electrolyte. The samples were directly clamped by electrode holder as a working electrode. The reversible hydrogen electrode (RHE) potential was calibrated by the measured potential according to the following equation:

$$E_{RHE} = E_{Ag/AgCl} + 0.1976 + 0.0591 \times pH$$

Before OER test, pure O$_2$ was purged into electrolyte to reach O$_2$-saturated condition. The O$_2$ flow was kept during the entire test process. The linear sweep voltammetry technique (LSV) was applied to record OER polarization curves at a scan rate of 1 mV s^{-1}, and the chronopotentiometry (CP) was used to measure the stability of the electrocatalysts at constant current densities of 10, 50 and 100 mA cm^{-2}, respectively. A wide frequency ranging (10 kHz − 100 mHz) with a current−voltage amplitude of 5 mV was applied for electrochemical impedance spectroscopy (EIS) at 1.52 V *vs.* RHE. Ohmic resistance was estimated from the EIS results at a phase angle of 0° in high frequency. The compensation was performed to all electrochemical performance results with 95% *iR* correction. Electrochemically active surface area (ECSA) was calculated by the following equation:

$$ECSA = C_{DL}/C_S$$

where C_{DL} is double layer capacitance, and C_S is specific capacitance. The roughness factor (RF) was calculated by the following equation:

$$RF = ECSA/A$$

where *ECSA* is the electrochemically active surface area, and *A* is the geometric area of electrode. The RF indicator can be used to evaluate the flatness of the electrochemical interface. Turnover frequency (TOF) was estimated from the following equation:

$$TOF = J \times A/4 \times n \times F$$

where *J* is the current density in OER polarization curves, *A* is geometric area of electrode, *F* is Faraday constant (C mol^{-1}), and *n* is mole number of active sites on the electrode. The reaction activation energy was based on the Arrhenius equation:

$$dIn(i)/d(1/T) = -E_{a,app}/R$$

where $E_{a,app}$ is the apparent activation energy, *R* is the gas constant, and *T* is the Kelvin temperature.

3. Results and discussion

Fig. 1a is the illustration of synthesizing Co_9S_8 nanoarrays with high electron deficiency by a "poor sulfur" hydrothermal strategy, where a limited amount (10 mg) of thiourea

(CH_4N_2S) is utilized to give poor sulfidation of Co foam (CF) in the formation of the resulting sample at 180 °C for 2 h. In contrast, the CoS nanoarrays have also been prepared only by changing the sulfur source to an excessive amount (20 mg) of sulfur powder for strong sulfidation under the same conditions (details in the Experimental section). Scanning electron microscope (SEM) and transmission electron microscope (TEM) techniques are deployed to characterize the morphology and microstructure of the resulting samples. From the SEM image of Fig. 1b, it is clearly visible that the resulting nanoarrays are tightly covered on Co foam surface with an average size of ~800 nm, which is favorable to enrich active sites and stabilize electron transportation at the electrochemical interface. Interestingly, when the sulfur source is changed to sulfur powder, the obtained morphology can keep fully covered nanoarrays except that the average size is increased to 1.5 μm (Fig. S1). Inset of Fig. 1b gives the wettability measurement of the resulting Co_9S_8 sample, showing droplet is much more easily absorbed by comparing with the pristine CF (Fig. S2). This great hydrophilicity is very helpful for electrolyte infiltration during OER. The TEM observations in Fig. S3 further characterized the resulting nanoarrays, showing the accordant results with the mentioned SEM images. The corresponding high-resolution TEM image (Fig. 1c) exhibits a planar spacing of 0.30 nm corresponding to Co_9S_8 (311) facet. Meanwhile, the verification of polycrystalline nature is provided by selected-area electron diffraction pattern (SAED,
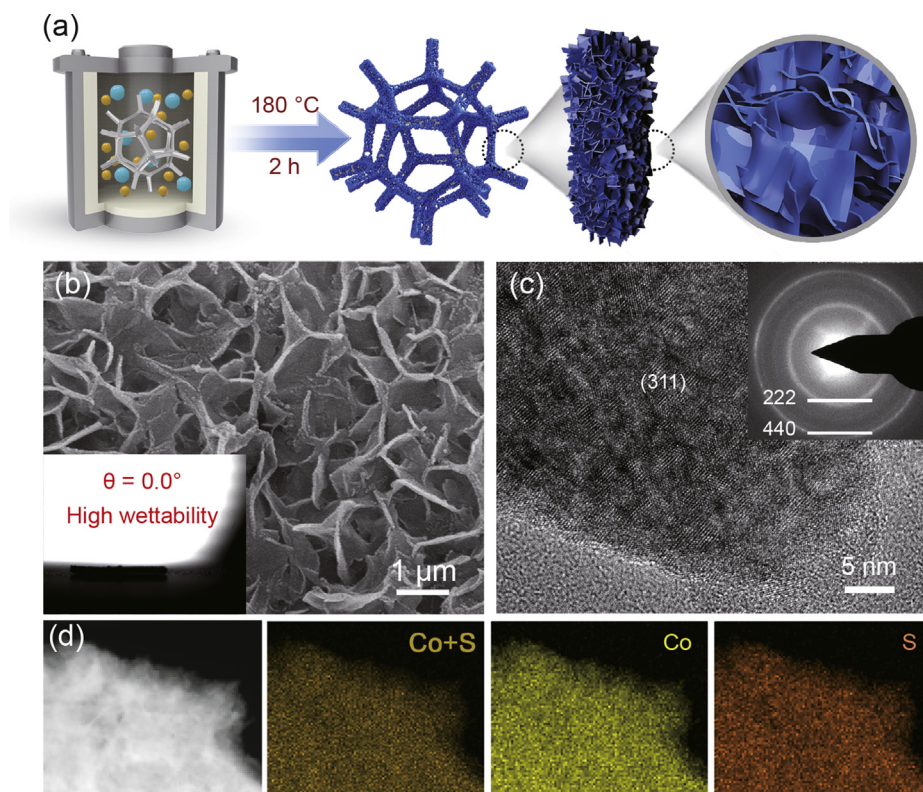

Fig. 1. (a) illustration of the synthesis of the highly surface electron-deficient Co_9S_8 nanoarrays; (b) SEM (*inset* showing the wettability measurement), (c) high-resolution TEM images (*inset* showing the corresponding SAED pattern), and (d) TEM-EDX mapping of the resulting Co_9S_8 nanoarrays.

inset of Fig. 1c), showing two diffraction rings indexed to the (222) and (440) faces. Element distribution of the Co_9S_8 nanoarrays is investigated *via* energy-dispersive X-ray spectroscopy (TEM-EDX), displaying homogenous existence of Co and S elements alone the entire structure, as shown in Fig. 1d.

Fig. 2a is the X-ray diffraction (XRD) patterns of the resulting samples. It can be seen that the poor sulfidation by thiourea can form Co_9S_8 (JCPDS: 02−1459) materials, which is in line with TEM results, while the strong sulfidation by sulfur powder generates CoS (JCSPDS: 02−0825) materials. The Raman spectra (Fig. 2b) show that the Co_9S_8 sample possesses similar peaks of Co−Co and weakened peaks of Co−S by comparing with the CoS, which is in accordance with previous literature [19,20]. To probe surface chemical states and compositions of the Co_9S_8 sample before OER, X-ray photoelectron spectroscopy (XPS) is performed with CoS as a control. As shown in Fig. 2c, Co 2p region of the Co_9S_8 can be fitted into six main peaks of Co $2p_{3/2}$ (777.9, 779.9, and 781.4 eV) and Co $2p_{1/2}$ (793.0, 795.7, and 797.0 eV) with two satellite peaks at 782.5 and 800.7 eV, indicating Co is in various chemical states with the percentage of 23% (Co^{3+}), 67% (Co^{2+}), and 10% (Co^0), respectively [21,22]. Notably, the content of Co^{3+} as active sites in the Co_9S_8 is much lower than that of the CoS (41%). Fig. 2d shows the S 2p region of the Co_9S_8 consisting of two peaks (161.8 eV; 163.4 eV) ascribed to S−Co and one peak (168.3 eV) attributed to S−O, respectively [23,24]. It is also noted that S−O content in the Co_9S_8 (31.1%) sample is greatly lower than that of CoS (50.1%), indicating more active S−Co in the Co_9S_8 will be involved in electrochemical process at the interface to activate valence electron of Co center [25,26]. More importantly, it is found that the Co_9S_8 gives relatively high BE of the Co sites. As shown in Fig. 2e, 781.6 and 779.9 eV are the values corresponding to Co^{2+} and Co^{3+}, conspicuously higher than all reported Co_9S_8-based materials. Such a fantastic phenomenon

implies high surface electron deficiency of the resulting Co_9S_8, which is highly essential for accelerating reaction kinetics to enhance OER performances. Element contents of the obtained samples are investigated using inductively coupled plasma mass spectrometry (ICP-MS). As shown in Fig. S4, the Co contents in the Co_9S_8 and CoS are 1.50 and 2.20 mg, while the corresponding S contents are 0.73 and 1.20 mg, respectively.

Evaluation of OER performances for the Co_9S_8 electrocatalysts is carried out in a standard three-electrode system with 1.0 M KOH as the electrolyte, where the commercial benchmark RuO_2, IrO_2, and CoS electrocatalysts are applied as controls (details in Experimental section). Fig. 3a are OER polarization curves of the resulting samples obtained by the linear sweep voltammetry technique at a sweep rate of 1 mV s^{-1}, exhibiting that the Co_9S_8 electrocatalysts only require ultrasmall overpotentials of 265, 311, and 326 mV to obtain the current densities of 10, 50, and 100 mA cm^{-2}, respectively, superior to those of commercial benchmark RuO_2, IrO_2, and CoS electrocatalysts. As shown in Fig. 3b, η_{50} and η_{100} of the resulting Co_9S_8 are certainly lower than those of the most representative literature, indicating the excellent OER performances in alkaline media. Moreover, high current densities of 500 and 1000 mA cm^{-2} can also be attained at low overpotentials of 370 and 420 mV (Fig. S5). These performances are beyond all other reported Co_9S_8-based electrocatalysts to date (Table S1). In order to estimate the number of active sites, the electrochemically active surface area (ECSA) and roughness factor (RF) are measured according to the calculated double-layer specific capacitance (Fig. S6 and S7). As shown in Fig. 3c, the ECSA and RF of the Co_9S_8 electrocatalysts are 59 cm^2 and 295, higher than those of the CoS (50 cm^2 and 250), implying the enrichment of catalytically active sites [27,28]. Furthermore, intrinsic activities of the Co_9S_8 electrocatalysts are investigated by calculating ECSA-, mass-normalized current densities and turnover frequencies. As shown in Fig. S8 and S9, the Co_9S_8 electrocatalysts give
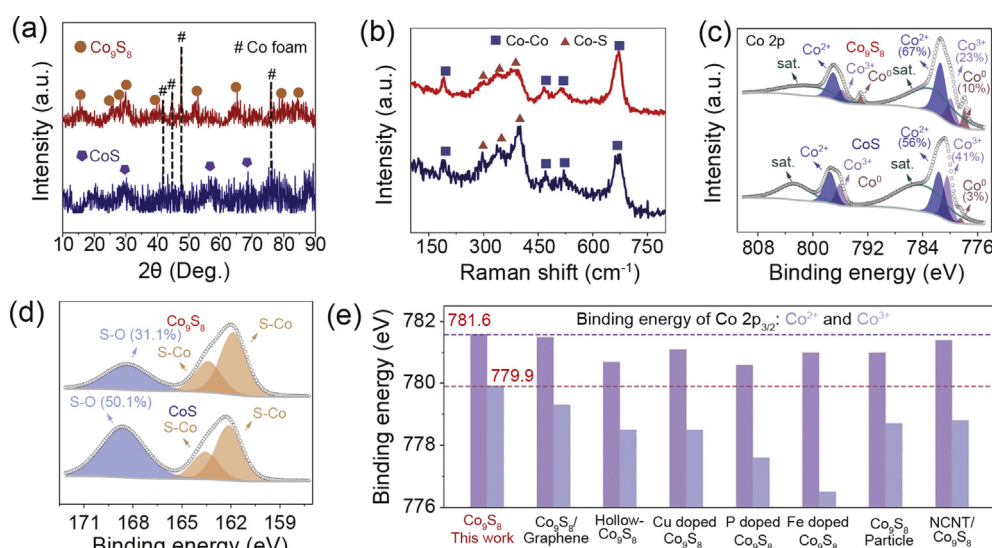

Fig. 2. (a) XRD patterns of the resulting Co_9S_8 and CoS; (b) Raman spectra of the resulting Co_9S_8 and CoS; XPS spectra of the resulting Co_9S_8 and CoS; (c) Co 2p and (d) O 1s regions; (e) comparisons of the Co $2p_{3/2}$ binding energies of the various reported Co_9S_8 electrocatalysts.
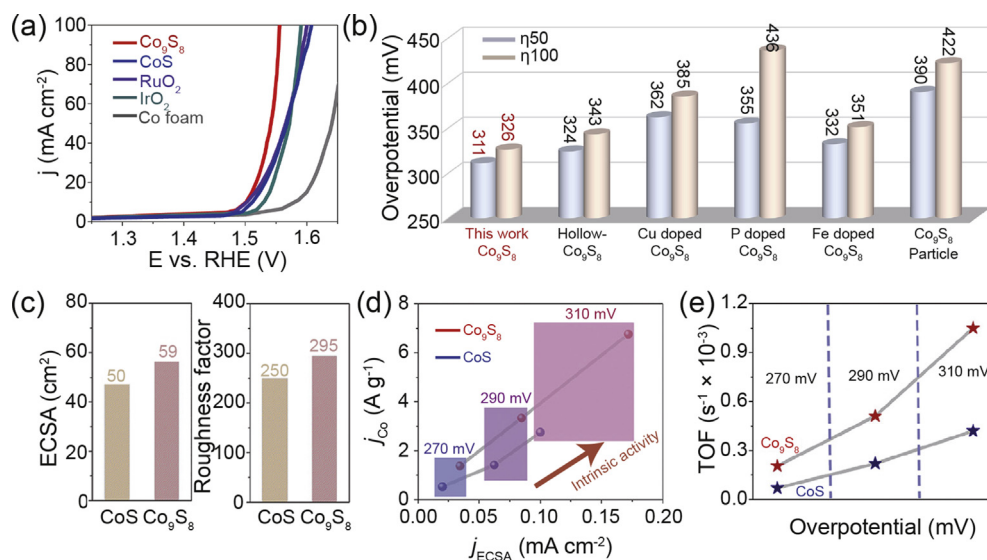
Fig. 3. (a) OER polarization curves of the Co_9S_8, CoS, commercial RuO_2/IrO_2 and Co foam; (b) comparisons of the overpotentials at current densities of 50 and 100 mA cm^{-2} of various reported Co_9S_8 electrocatalysts; (c) electrochemically active surface area and roughness factor of the resulting Co_9S_8 and CoS; comparisons of (d) ECSA-normalized activities, mass activities and (e) turnover frequencies of the resulting Co_9S_8 and CoS at various current densities, respectively.

higher ECSA- and mass-normalized current densities of 0.17 mA cm^{-2} and 6.76 A g^{-1} at the overpotential of 310 mV, much higher than those of CoS (0.09 mA cm^{-2}; 2.03 A g^{-1}). The comprehensive comparison of these two indicators is provided in Fig. 3d. It can be seen that the augment of ECSA- and mass-normalized current densities for Co_9S_8 are more significant than those of the CoS, implying the dramatically enhanced OER kinetics. A similar trend can also be observed

from the comparison of turnover frequencies (TOF) for these two samples. As shown in Fig. 3e and Fig. S10, TOF values of the Co_9S_8 electrocatalysts are markedly higher than those of CoS at various overpotentials. Especially at 310 mV, the corresponding value is 1.03 s^{-1}, 2.5 times higher than that of CoS (0.40 s^{-1}).

For an in-depth assessment of OER kinetics, the Tafel slopes of the resulting samples are calculated to compare the
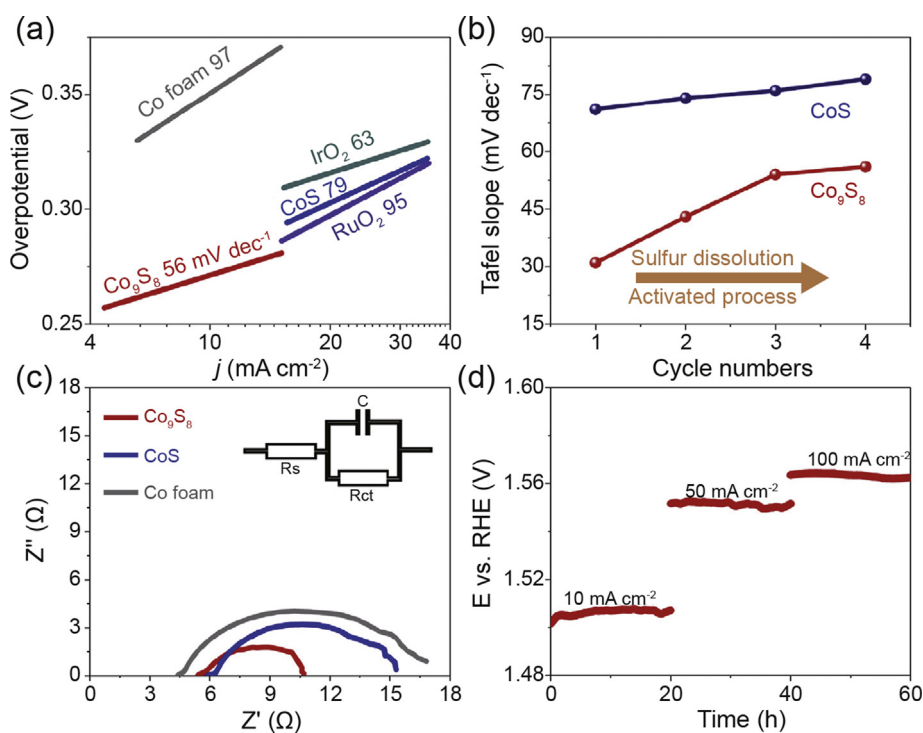

Fig. 4. (a) Tafel plots of the Co_9S_8, CoS, commercial RuO_2/IrO_2 and Co foam; (b) dynamic Tafel slope evolution and (c) Nyquist plots of the resulting Co_9S_8 and CoS; (d) chronopotentiometry response of the resulting Co_9S_8 at 10, 50 and 100 mA cm^{-2}, respectively.
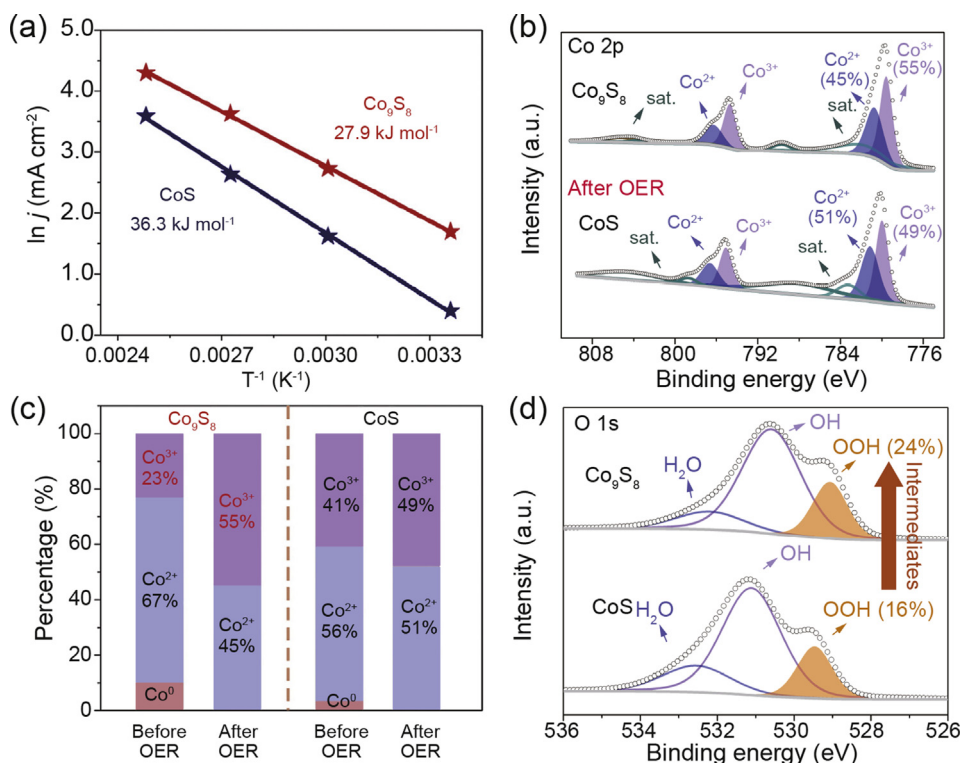
Fig. 5. (a) Arrhenius plots of the resulting Co_9S_8 and CoS at an overpotential of 230 mV; (b) XPS spectra of Co 2p region of the Co_9S_8 after OER and (c) the corresponding chemical state distributions; (d) XPS spectra of S 2p region of the Co_9S_8 after OER.

change rate of current density with an increase of over-potentials. As shown in Fig. 4a, the value of Co_9S_8 electro-catalysts is 56 mV dec^{-1}, which is the smallest one in comparison to RuO_2 (95 mV dec^{-1}), IrO_2 (63 mV dec^{-1}), and CoS (79 mV dec^{-1}) electrocatalysts, confirming the improved kinetics caused by high electron deficiency of the Co center. To unravel the detailed impact on reaction kinetics, four initial OER polarization curves of the Co_9S_8 are recorded to inves-tigate the variation of Tafel value with the CoS as a control (Fig. S11 and S12). Noteworthily, significant change can be observed for the Co_9S_8, giving an increasing trend from 31 mV dec^{-1} at the first scan to 56 mV dec^{-1} at the fourth scan. In contrast, the value for the CoS is negligibly increased from 71 mV dec^{-1} to 79 mV dec^{-1}, as shown in Fig. 4b. Therefore, it can be concluded that the highly deficient Co center in the Co_9S_8 can effectively activate chemical states at the electrochemical interface to accelerate the OER kinetics. This is also verified by the corresponding Nyquist plots that quantify the solution resistance (R_s) and interfacial charge transfer resistance (R_{ct}) relevant to the high- and low-frequency responses during OER [29,30]. As shown in Fig. 4c, R_{ct} of the Co_9S_8 electrocatalysts is 5.1 Ω, also the smallest value compared with the CoS (9.3 Ω) and the CF (16.7 Ω). In addition, catalytic stability is another important indicator of evaluating catalytic performances. Fig. 4d is the chronopotentiometric measurement (CP) curve of the Co_9S_8 measured in O_2-saturated 1.0 M KOH, which only shows slight potential drops during a 60 h long-term test, indicating

excellent stability even under various current densities (10, 50, and 100 mA cm^{-2}).

To gain deeper insight into the valence electron defi-ciency effect on OER process, the kinetic energy barriers of the Co_9S_8 and CoS electrocatalysts are estimated by measuring the polarization curves at the different temper-atures (Fig. S13, details in Experimental section). From the Arrhenius plot of Fig. 5a, it can be seen that apparent activation energy ($E_{a,app}$) of the Co_9S_8 is 27.9 kJ mol^{-1}, obviously smaller than that of the CoS (36.3 kJ mol^{-1}), implying that high electron deficiency can endow the Co_9S_8 with more rapid reaction rate than that of the CoS [31]. Furthermore, XPS techniques are applied to probe the chemical state variation of Co_9S_8 electrocatalysts after OER, where the CoS is utilized as a referenced control. For attaining a steady surface state, the samples were used to catalyze OER at an overpotential of 270 mV for 6 h before XPS test. It has been evidenced theoretically and experimentally that the enrichment of Co^{3+} is greatly vital to optimize the adsorption of key intermediates during OER for boosting catalytic performances [32−34]. As shown in Fig. 5b and c, the content of Co^{3+} in the Co_9S_8 is significantly increased from 23% to 55% after OER, while the value in the CoS is slightly changed from 41% to 51%. At the meantime, the corresponding O 1s spectra (Fig. 5d) display that OOH* content of the Co_9S_8 reaches 22%, nearly 1.4 times higher than that of CoS (16%). Such intriguing phenomena verified that high electron deficiency

can engender Co center to enrich more Co^{3+} at the interface, thus effectively optimizing the adsorption of key OOH* intermediates. This feature can largely speed up the reaction kinetics to minimize the overpotential with enhanced intrinsic and apparent activities.

4. Conclusions

In summary, we have demonstrated the synthesis of highly surface electron-deficient Co_9S_8 nanoarrays by a "poor sulfur" hydrothermal method. The resulting Co_9S_8 exhibits the highest BE of Co center in comparison with the reported Co_9S_8-based materials, leading to a relatively low reaction activated energy (27.9 kJ mol^{-1}) and abundant OOH* key intermediates (24%). Consequently, ultrasmall overpotentials of 265 and 326 mV are required to deliver the current densities of 10 and 100 mA cm^{-2}, respectively, surpassing commercial benchmark RuO_2/IrO_2 catalysts and most of the reported Co_9S_8-based materials in alkaline media. The corresponding Tafel slope is as low as 56 mV with a slight overpotential fading after 60 h long-term stability measurement. Meanwhile, the resulting Co_9S_8 electrocatalysts also exhibit exceptional intrinsic OER activities, giving the much higher mass, ECSA-normalized activities, and TOF values of 6.76 A g^{-1}, 0.17 mA cm^{-2}, and 1.05 s^{-1} than those of CoS (2.75 A g^{-1}; 0.10 mA cm^{-2}; 0.42 s^{-1}) at the overpotential of 310 mV, respectively. This work realized high electron deficiency of Co_9S_8 materials can guide the further exploitation of other non-noble electrocatalysts.

Conflict of interest

The authors declare there are no conflicts of interest.

Appendix A. Supplementary data

Supplementary data to this article can be found online at https://doi.org/10.1016/j.gee.2020.07.010.

References

[1] Z.W. Seh, J. Kibsgaard, C.F. Dickens, I.B. Chorkendorff, J.K. Norskov, T.F. Jaramillo, Science 355 (2017) eaad4998.
[2] Y. Peng, S. Chen, Green Energy Environ. 3 (2018) 335−351.
[3] Q.C. Xu, H. Jiang, H.X. Zhang, Y.J. Hu, C.Z. Li, Appl. Catal., B 242 (2019) 60−66.
[4] H. Zhang, H. Jiang, Y. Hu, H. Jiang, C. Li, Green Energy Environ. 2 (2017) 112−118.
[5] S.H. Ye, Z.X. Shi, J.X. Feng, Y.X. Tong, G.R. Li, Angew. Chem. Int. Ed. 57 (2018) 2672−2676.
[6] H.S. Oh, H.N. Nong, T. Reier, A. Bergmann, M. Gliech, J.F. de Araujo, E. Willinger, R. Schlogl, D. Teschner, P. Strasser, J. Am. Chem. Soc. 138 (2016) 12552−12563.
[7] S. Cherevko, S. Geiger, O. Kasian, N. Kulyk, J.P. Grote, A. Savan, B.R. Shrestha, S. Merzlikin, B. Breitbach, A. Ludwig, K.J.J. Mayrhofer, Catal. Today 262 (2016) 170−180.
[8] W.J. Jiang, T. Tang, Y. Zhang, J.S. Hu, Acc. Chem. Res. 53 (2020) 1111−1123.
[9] L. Li, P. Wang, Q. Shao, X. Huang, Chem. Soc. Rev. 49 (2020) 3072−3106.
[10] S. Peng, F. Gong, L. Li, D. Yu, D. Ji, T. Zhang, Z. Hu, Z. Zhang, S. Chou, Y. Du, S. Ramakrishna, J. Am. Chem. Soc. 140 (2018) 13644−13653.
[11] Y. Wang, C. Xie, Z. Zhang, D. Liu, R. Chen, S. Wang, Adv. Funct. Mater. 28 (2018) 1703363.
[12] C. Li, Z. Luo, T. Wang, J. Gong, Adv. Mater. 30 (2018) 17007502.
[13] H. Zhu, J. Zhang, R. Yanzhang, M. Du, Q. Wang, G. Gao, J. Wu, G. Wu, M. Zhang, B. Liu, J. Yao, X. Zhang, Adv. Mater. 27 (2015) 4752−4759.
[14] M. Al-Mamun, Y. Wang, P. Liu, Y.L. Zhong, H. Yin, X. Su, H. Zhang, H. Yang, D. Wang, Z. Tang, H. Zhao, J. Mater. Chem. 4 (2016) 18314−18321.
[15] D. Xiong, Q. Zhang, S.M. Thalluri, J. Xu, W. Li, X. Fu, L. Liu, Chem. Eur J. 23 (2017) 8749−8755.
[16] H. Qian, J. Tang, Z. Wang, J. Kim, J.H. Kim, S.M. Alshehri, E. Yanmaz, X. Wang, Y. Yamauchi, Chem. Eur J. 22 (2016) 18259−18264.
[17] J. Yang, G.X. Zhu, Y.J. Liu, J.X. Xia, Z.Y. Ji, X.P. Shen, S.K. Wu, Adv. Funct. Mater. 26 (2016) 4712−4721.
[18] S. Deng, Y. Zhong, Y. Zeng, Y. Wang, X. Wang, X. Lu, X. Xia, J. Tu, Adv. Sci. 5 (2018) 1700772.
[19] W. Li, Y. Li, H. Wang, Y. Cao, H. Yu, F. Peng, Electrochim. Acta 265 (2018) 32−40.
[20] P.F. Yin, L.L. Sun, Y.L. Gao, S.Y. Wang, Bull. Mater. Sci. 31 (2008) 593−596.
[21] M.C. Biesinger, B.P. Payne, A.P. Grosvenor, L.W.M. Lau, A.R. Gerson, R.S.C. Smart, Appl. Surf. Sci. 257 (2011) 2717−2730.
[22] H. Zhang, B. Chen, H. Jiang, X. Duan, Y. Zhu, C. Li, Nanoscale 10 (2018) 12991−12996.
[23] H. Vrubel, D. Merki, X. Hu, Energy Environ. Sci. 5 (2012) 6136−6144.
[24] T. Yokoyama, A. Imanishi, S. Terada, H. Namba, Y. Kitajima, T. Ohta, Surf. Sci. 334 (1995) 88−94.
[25] Y. Li, W. Zhou, J. Dong, Y. Luo, P. An, J. Liu, X. Wu, G. Xu, H. Zhang, J. Zhang, Nanoscale 10 (2018) 2649−2657.
[26] Z. Xiao, G. Xiao, M. Shi, Y. Zhu, ACS Appl. Mater. Interfaces 10 (2018) 16436−16448.
[27] H. Zhang, H. Jiang, Y. Hu, P. Saha, C. Li, Mater. Chem. Front. 2 (2018) 1462−1466.
[28] Y. Pi, N. Zhang, S. Guo, J. Guo, X. Huang, Nano Lett. 16 (2016) 4424−4430.
[29] Y. Meng, W. Song, H. Huang, Z. Ren, S.Y. Chen, S.L. Suib, J. Am. Chem. Soc. 136 (2014) 11452−11464.
[30] Q. Xu, H. Jiang, Y. Li, D. Liang, Y. Hu, C. Li, Appl. Catal., B 256 (2019). UNSP117893.
[31] L. Li, H. Yang, J. Miao, L. Zhang, H.Y. Wang, Z. Zeng, W. Huang, X. Dong, B. Liu, ACS Energy Lett. 2 (2017) 294−300.
[32] Y. Surendranath, M. Dinca, D.G. Nocera, J. Am. Chem. Soc. 131 (2009) 2615−2620.
[33] L. Zhuang, L. Ge, Y. Yang, M. Li, Y. Jia, X. Yao, Z. Zhu, Adv. Mater. 29 (2017) 1606793.
[34] T.W. Kim, M.A. Woo, M. Regis, K.S. Choi, J. Phys. Chem. Lett. 5 (2014) 2370−2374.